Brodogradnja Volume 77 Number 3 (2026) 77313

journal homepage: www.brodogradnja.fsb.hr

Brodogradnja

An International Journal of Naval Architecture and Ocean Engineering for Research and Development

Safety assessment of moray base floating wind turbine foundation with steel–UHPC material through CFD–FEA method

Fali Huo[1], *Guojian Lv*[1], *Jianjie Niu*[1,*], *Jichuan Yang*[2], *Ping Luo*[3]

[1] *School of Naval Architecture and Ocean Engineering, Jiangsu University of Science and Technology, Zhenjiang 212100, China*
[2] *Shanghai Salvage Bureau, Ministry of Transport of the People's Republic of China, Shanghai 200090, China*
[3] *Nantong Just-Sea Offshore Equipment Co., Ltd., Nantong 226100, China*

ARTICLE INFO

Keywords:
Floating wind turbine
UHPC
CFD–FEA method
Structural strength
Tank experiment

ABSTRACT

In this study, a floating offshore wind turbine with a foundation constructed from steel–UHPC (ultrahigh performance concrete) is investigated. The structural design and strength performance of the floating foundation are evaluated through a combination of numerical simulation and wave tank experiments. Load assessment and feasibility analyses, which reveal that the proposed steel–UHPC foundation satisfies structural safety requirements while exhibiting significant potential for material cost reduction, are conducted. With respect to the numerical simulation, a coupling of computational fluid dynamics (CFD) and finite element analysis (FEA) solvers is employed to address the fluid–structure interaction (FSI) problem. External hydrodynamic pressure obtained from the CFD solver is used to derive the structural response in the FEA solver. Given that the deformation of the steel–UHPC structure has a negligible effect on the surrounding flow field, one-way CFD–FEA coupling, in which fluid loads are transferred to the structural model without feedback of structural deformation to the fluid solver, is used. Wave tank experiments are conducted to validate the accuracy and reliability of the proposed one-way coupling methodology. Furthermore, an equivalent constitutive model for steel–UHPC is implemented within the FEA solver. The corresponding physical and mechanical properties are derived, and key structural design parameters of the floating foundation are determined accordingly.

1. Introduction

Floating wind turbine foundations are critical in maintaining offshore wind energy systems. However, conventional steel floating foundations typically require 700–1000 tons of steel per megawatt, resulting in high costs [1]. This limitation highlights the need for structural optimization and the use of cost-effective alternative materials to enhance economic viability. Recent advances in concrete technology have resulted in significant developments in structural engineering applications [2]. Ultrahigh performance concrete (UHPC) has outstanding properties, including compressive strength exceeding 150 MPa and excellent resistance to environmental corrosion [3]. The superior durability and mechanical properties of UHPC enable its

* Corresponding author.
E-mail address: niujianjie1989@163.com

https://doi.org/10.21278/brod77313
Received 18 August 2025; Received in revised form 17 January 2026; Accepted 18 January 2026
Available online 9 February 2026
ISSN 0007-215X; eISSN 1845-5859

application in advanced infrastructure, especially in offshore engineering, reducing maintenance demands and improving constructability [4]. Despite these advantages, limited research has focused on floating wind turbine foundations constructed using steel–UHPC. Therefore, this study proposes a steel–UHPC-based structural design for floating wind turbine foundations. The thickness and reinforcement characteristics of each component are designed. The FEA solver is used to calculate the equivalent constitutive model and physical properties of steel-UHPC components. The CFD–FEA method is used to analyse its structural strength and evaluate its safety.

In terms of material application, early studies focused on the use of conventional steel or ordinary concrete in marine structures. For example, Nie [5] designed an ultralarge steel–concrete composite structural floating platform for the ocean that is adapted to the requirements of constructing ultralarge floating platforms at sea. The research findings indicate that this design increases the resistance of the structure to fire, blast, and impact, simultaneously improving the stability and durability of the components. Moreover, the design substantially reduces the consumption of structural steel. With the emergence of UHPC, scholars began to explore its potential in marine engineering. Zheng et al. [6] used basalt fibre material as the basis for the structural design of a net cage and analysed the structural strength and hydrodynamic performance of an ocean net box by using the fluid structure coupling calculation method. Zeng et al. [7] systematically reviewed the durability of UHPC under various environmental conditions, such as seawater corrosion, chloride penetration, and freeze thaw cycles. This review provides experimental evidence supporting the applicability of UHPC in floating foundations. In this study, the floating platform of the wind turbine is directly submerged in seawater, which constitutes a highly corrosive environment. Walia et al. [8] further proposed the use of prefabricated UHPC components in tension leg platforms (TLPs), which can reduce the cost by approximately 90 % and the steel consumption by 95 % compared with steel foundations. Yan et al. [9] proposed improving the compressive performance of 3D-printed UHPC elements by wrapping them with fibre-reinforced polymer (FRP). Axial compression tests on FRP-confined, 3D-printed UHPC and unconfined 3D-printed UHPC cylinders were conducted. Yao et al. [4] proposed an analytical model to predict the flexural behaviour of hybrid reinforced UHPC with steel reinforcements. By considering the interactions of reinforcing mechanisms, the proposed model may be useful in the selection of performance design parameters to achieve optimal results with minimal use of materials. Hussain et al. [10] developed a nanocarbon black-UHPC with self-sensing function, which provides a new material solution for marine structural health monitoring. This is a significant advancement in the field of ocean engineering. UHPC has significant potential in marine engineering because of its excellent mechanical properties and durability, and studies have explored its use in floating structures such as TLPs. However, most of these studies focus on the performance of the material itself or simplified structural concepts. With respect to complex semisubmersible floating wind turbine foundations, systematic investigations spanning constitutive material modelling, detailed structural design, and experimental validation remain scarce.

Recent advancements in computational technology have resulted in substantial progress in numerical simulation methods for marine engineering applications. These computational techniques have become indispensable for resolving complex FSI phenomena in offshore environments. Early studies primarily relied on simplified models or one-way coupling. With higher computing power, the method is gradually developing into high fidelity and two-way coupling. Jiao et al. [11] investigated slamming behaviour and structural response of ship structures by CFD–FEA method, enabling prediction of stiffened hull plate loads for structural design. Chen et al. [12] further applied the method to analyse wave and slamming loads of multiscale ships and discussed the scale effect. Researchers have indicated that compared with the vertical motion, the scale effect on the slamming pressure load is more significant than that of a ship. Jiao et al. [13] used CFD–FEA coupling simulation method to analyse the comprehensive motion, wave load, slamming and upwash pressure of ships under different regular wave conditions. The results revealed that the CFD–FEA coupling method can accurately simulate the wave resistance, wave load, slamming pressure and upwash pressure of flexible ships sailing in regular waves. With respect to specific applications, Jia et al. [14] used CFD method to numerically simulate the hydrodynamic interaction between wave-induced LNG ship motion and liquid cargo tank sloshing behaviour. In terms of the design and evaluation of liquid cargo ships, it is very important to consider the coupling effect of tank sloshing and ship dynamics. Kale et al.

[15] investigated the hydrodynamic performance of a horizontal axis turbine through combined experimental testing and the CFD method. The results revealed that the relative error of the separated eddy simulation model is smaller than that of other turbulence models at the same tip speed, and the results of the sliding mesh method, which describes rotation, are closer to the experimental results in the study of the y+ angle. Lakshmynarayanan et al. [16, 17] employed one-way and two-way CFD–FEA coupling methods to investigate the symmetric motions and loads of the S175 container ship under strong waves and slamming. Li et al. [18] reviewed the numerical strategy of ship hydroelasticity on the basis of CFD–FEM technology, whereas Löhner et al. [19] focused on increasing the application range of one-way coupling and verifying its reliability. These studies reveal that the CFD–FEA coupling method has become a powerful tool for solving complex fluid–solid coupling problems in marine engineering, and its reliability has been widely validated. In terms of experimental validation, wave tank experiments and physical model tests are indispensable for validating numerical methods and evaluating structural performance, particularly under complex environmental loading. Ding et al. [20] employed a solid model on the basis of the implicit DEM method and the DDA technique to investigate the stability of breakwaters under strong wave impacts via a triple-coupled flow porosity solid model. Lin et al. [21] systematically investigated the dynamic response and safety of large marine structures under combined loading conditions. To achieve this, a three-dimensional numerical wave tank including a conduit rack platform was constructed using CFD software Fluent, and the fluid–structure coupling between the wave and the platform was simulated numerically. Yu et al. [22] calculated the relevant hydrodynamic coefficients of diverse vessel models at different drop angles through computational fluid dynamics methods. A comparison between the drop test results and the CFD simulation results revealed the validity of the CFD-derived results, including the total flow time, landing position, and number of spatial overturning events. Yin et al. [23] proposed a bottom articulated flip flop breakwater aimed at wave attenuation and coastal protection. A series of indoor tests and CFD numerical modelling were conducted to explore the hydrodynamic characteristics under regular waves. Hydrodynamic coefficients, maximum point pressure, and mean pitch amplitude of the flaps were analysed in relation to the incident wave parameters and the flap characteristics. By employing a two-dimensional, Reynolds-averaged Navier–Stokes CFD model, Jiang et al. [24] investigated the effect of adjacent floats on the hydrodynamic coefficients of floats and wave loads. These experimental studies not only validate numerical models but also better elucidate response mechanisms under realistic environmental loading conditions.

Although the above review highlights the progress of UHPC application and CFD–FEA technology, there are still significant research gaps in the integrated design, analysis and experimental verification of steel–UHPC hybrid floating foundations for offshore wind turbines. Existing research focuses on traditional steel structural design or UHPC in other marine engineering contexts. However, comprehensive research on material constitutive modelling, detailed structural design, coupled numerical simulations, and wave tank experiments for semisubmersible floating foundations remains limited. To address these gaps, a safety assessment of a Moray Base floating wind turbine foundation constructed with steel–UHPC composite materials under extreme wave conditions was performed in this study. In this study, numerical simulations are systematically integrated with wave tank experiments.

The new contributions of this study are summarized as follows:

1. A steel–UHPC composite concept is proposed and applied to a semisubmersible floating wind turbine foundation, and a complete structural design featuring differentiated plate thickness and reinforcement layouts tailored for the marine environment is developed.

2. An equivalent constitutive model of steel–UHPC members is developed, enabling efficient and accurate global strength analysis within the framework of finite element analysis and avoiding the computational cost of simulating detailed steel–concrete interactions.

3. A validated one-way CFD–FEA coupling framework is established to assess the wave loads and global structural responses of the proposed foundation under extreme wave conditions, and its accuracy is verified through dedicated wave tank experiments.

4. A direct comparative analysis is conducted to preliminarily evaluate the economic and structural performance of the steel–UHPC design over the traditional all-steel design with the same floating body configuration, revealing significant material cost reductions while maintaining structural safety.

The findings of this study provide an important reference for the design of cost-effective and durable floating foundations and contribute to the advancement of marine renewable energy.

2. Theory and solution method

2.1 Flow field control equation

In a CFD–FEA framework, the governing equations of the fluid domain interact with those of the solid domain through a coupled interface. The fluid governing equations compute the hydrodynamic forces exerted by the fluid on the solid structure. The pressure, shear stress, and other loads acting on the solid boundary are derived from the fluid flow solution:

$$\frac{\partial \rho}{\partial t} + \nabla \cdot (\rho \mathbf{v}) = 0 \tag{1}$$

where ρ represents density, $\mathbf{v}$ denotes velocity vector, and velocity components are (u, v, w).

The transformed continuity equation, which is on the basis of conservation of mass, is expressed as follows:

$$\frac{\partial (\rho \mathbf{v})}{\partial t} + \nabla \cdot (\rho \mathbf{v}\mathbf{v}) = \nabla \cdot \boldsymbol{\sigma} + \rho \mathrm{g} \tag{2}$$

where $\boldsymbol{\sigma}$ represents stress tensor and g denotes acceleration of gravity.

The stress tensor of a fluid is typically expressed as the sum of normal stress and shear stress: $\boldsymbol{\sigma} = -p\mathbf{I} + \mathbf{T}$; this can be obtained by substituting the given expression into Equation 2:

$$\frac{\partial (\rho \mathbf{v})}{\partial t} + \nabla \cdot (\rho \mathbf{v}\mathbf{v}) = -\nabla \cdot (p\mathbf{I}) + \nabla \cdot \mathbf{T} + \rho g \tag{3}$$

where p represents pressure, $\mathbf{I}$ denotes unit tensor, and $\mathbf{T}$ indicates viscous stress tensor.

2.2 Newmark method

On the basis of the related study of Xia et al. [25], the generalized kinematic equations of the structural system are shown below:

$$\mathbf{M}\ddot{\mathbf{U}} + \mathbf{C}\dot{\mathbf{U}} + \mathbf{K}\mathbf{U} = \mathbf{R_t} \tag{4}$$

where **M**, **C** and **K** represent the mass matrix, damping matrix and tangent stiffness matrix, respectively, and $\mathbf{R_t}$ denotes the external load matrix.

They are the displacement, velocity and acceleration of the object at a specific moment. In this study, the finite element calculation used in the fluid–structure coupling analysis of a floating wind turbine is a nonlinear dynamic strength problem. Considering the variability of the modes of the object with the structure, the Newmark method of direct integration is used. Here, the state of the object at the moment is related not only to the moment t but also to specific physical quantities at the moment $t + \Delta t$. Assuming that the acceleration of the object changes linearly during the time interval $[t, t + \Delta t]$, the velocity and displacement of the object at time $t + \Delta t$ are as follows:

$$\dot{\mathbf{U}}_{\mathbf{t+\Delta t}} = \dot{\mathbf{U}}_{\mathbf{t}} + [(1-\delta)\ddot{\mathbf{U}}_{\mathbf{t}} + \delta \ddot{\mathbf{U}}_{\mathbf{t+\Delta t}}]\Delta t \tag{5}$$

$$\mathbf{U_{t+\Delta t}} = \mathbf{U_t} + \dot{\mathbf{U}}_\mathbf{t}\Delta t + [(\frac{1}{2} - \alpha)\ddot{\mathbf{U}}_\mathbf{t} + \delta\ddot{\mathbf{U}}_\mathbf{t+\Delta t}]\Delta t^2 \tag{6}$$

With these equations, expressions for $\ddot{\mathbf{U}}_\mathbf{t+\Delta t}$ and $\dot{\mathbf{U}}_\mathbf{t+\Delta t}$ in terms of $\mathbf{U_{t+\Delta t}}$, $\dot{\mathbf{U}}_\mathbf{t}$ and $\ddot{\mathbf{U}}_\mathbf{t}$ can be derived. These expressions can subsequently be integrated into the kinematic equations:

$$\hat{\mathbf{K}}\mathbf{U_{t+\Delta t}} = \hat{\mathbf{R}}_\mathbf{t+\Delta t} \tag{7}$$

where:

$$\hat{\mathbf{K}} = \frac{1}{\alpha\Delta t^2}\mathbf{M} + \frac{\delta}{\alpha\Delta t}\mathbf{C} + \mathbf{K} \tag{8}$$

$$\begin{aligned}\hat{\mathbf{R}}_\mathbf{t+\Delta t} = \mathbf{R_{t+\Delta t}} + \mathbf{M}[&\frac{1}{\alpha\Delta t^2}\mathbf{U_t} + \frac{1}{\alpha\Delta t}\dot{\mathbf{U}}_\mathbf{t}(\frac{1}{2\alpha} - 1)\ \ddot{\mathbf{U}}_\mathbf{t}] + \\ \mathbf{C}[&\frac{\delta}{\alpha\Delta t}\mathbf{U_t} + (\frac{\delta}{\alpha} - 1)\ \dot{\mathbf{U}}_\mathbf{t} + (\frac{\delta}{2\alpha} - 1)\ \Delta t\ddot{\mathbf{U}}_\mathbf{t}]\end{aligned} \tag{9}$$

where $\hat{\mathbf{K}}$ represents effective stiffness matrix and $\hat{\mathbf{R}}_\mathbf{t+\Delta t}$ denotes payload vector.

The effective stiffness matrix is depicted in the aforementioned equation, and the current $\mathbf{R_{t+\Delta t}}$ is used to determine the current moment $\mathbf{U_{t+\Delta t}}$. When the load history is known, $\mathbf{R_{t+\Delta t}}$ is a known quantity, and the kinematic equations can be resolved through iteration.

2.3 FSI analysis method

Walia et al. [8] proposed the application of UHPC for TLPs and reported, through one-way coupled CFD–FEA, that the structural deformation remained below 0.1 m (strain <0.05 %) under wave loading. This finding confirms the applicability of one-way coupling under small deformation. Jiao et al. [13] compared the accuracy of one-way/two-way coupling in terms of ship slamming load and reported that the pressure deviation of one-way coupling of a UHPC structure is less than 8 %, and the calculation efficiency is improved by 4 times, which is suitable for quasibrittle materials (such as UHPC). Wijesooriya et al. [26] reported that the deviation introduced by one-way coupling is controllable (stress deviation <3 %) under small-deformation conditions (strain <0.2 %), which are well suited for the analysis of UHPC structures. The steel–UHPC floating platform investigated in this study adopts high–strength materials, and the strain levels expected under extreme wave loading are well below this threshold (a conclusion that will be quantitatively verified by the calculated results presented in Section 4.7). Therefore, the use of a one-way coupling approach for the numerical simulations in this study is considered reasonable.

The one-way coupling model operates under the assumption that fluid–solid interactions are negligible, which simplifies the computational framework. The specific process is described as follows: First, the boundary conditions obtained from the fluid-domain simulation, including pressure and shear stress, are transferred to the structural model. Second, the stress–strain analysis of the solid structure is performed on the basis of the received loads to obtain the corresponding deformation response. Third, the deformation results are not fed back to the fluid domain, and the fluid remains unaffected by the deformation of the solid. Figure 1 presents the flow chart of the CFD–FEA numerical simulation process.

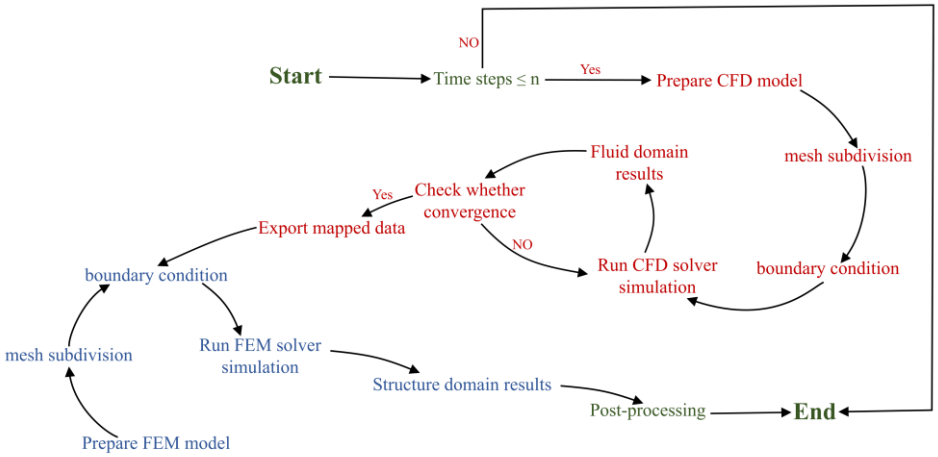

Fig. 1 Simulation process of one-way coupled model

3. Numerical modelling and meshing

3.1 Model description

The structural design of the Moray Base floating wind turbine considers the sea conditions of the designated installation site, as well as the platform characteristics and wind turbine configuration. The platform is constructed using steel–UHPC, a material selected for its excellent adaptability to maritime environments. The Moray Base floating wind turbine consists of a heave plate, a floating platform, a tower, a nacelle, a hub, and blades. The main scale parameters are shown in Figure 2. The main scales are listed in Table 1, and the hydrostatic parameters of the floating wind turbine are presented in Table 2. On the basis of the basic scale parameters of the floating wind turbine, hydrodynamic modelling is performed, and the hydrodynamic model and its grid division are shown in Figure 3.

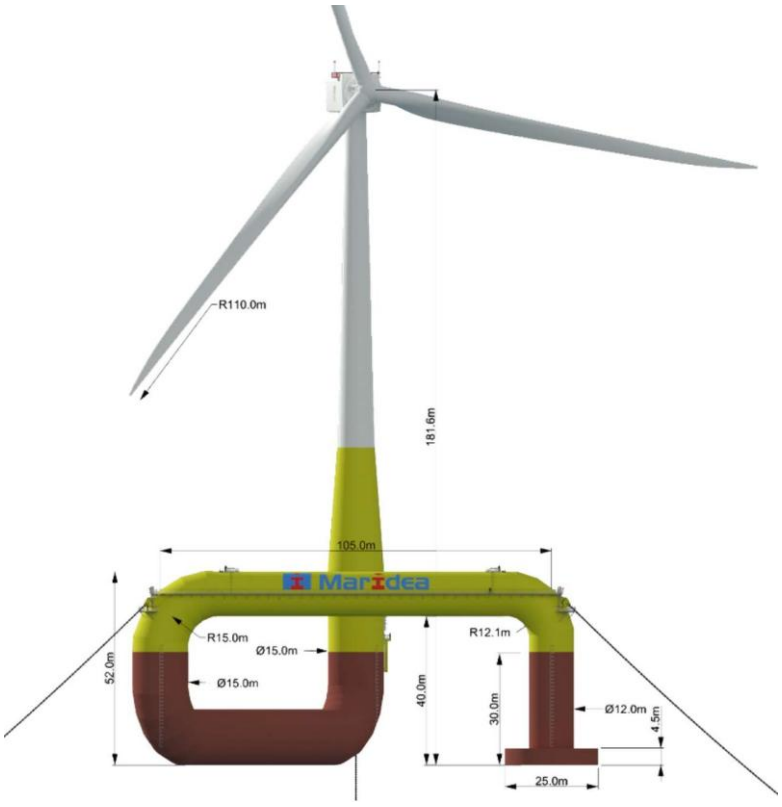

Fig. 2 Main scale parameters of the Moray Base (source: index, Maridea BV)

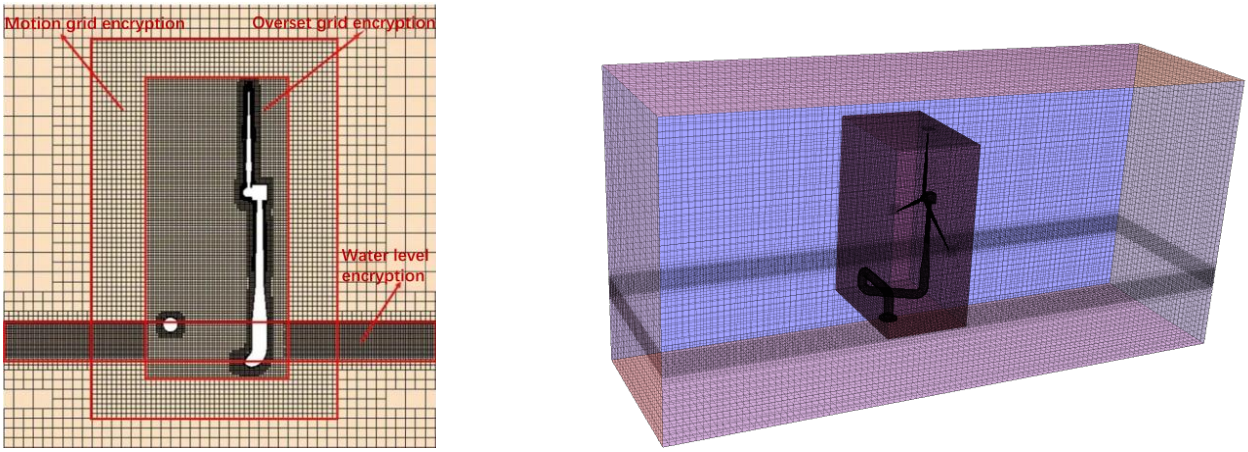

(a) Grid encryption at each location (b) CFD model of the Moray Base

Fig. 3 CFD modelling and meshing of the Moray Base

Table 1 Principal dimensions of the Moray Base

Parameter	Value
Total length (m)	106
Total width (m)	120
Total height of the floating body (m)	53.5
Diameter of the floating body (m)	15
Diameter of the heave plate (m)	30
Height of the hub (m)	181.6
Blade (m)	110
Displacement (t)	31452.2

Table 2 Hydrostatic parameters of the Moray Base

Centre of gravity (m)			Moment of inertia (kg×m^2)		
L_{CG}	T_{CG}	V_{CG}	I_{xx}	I_{yy}	I_{zz}
-35.71	-9.32	28.36	9.897×10^{10}	1.047×10^{11}	7.566×10^{10}

3.2 Numerical tank creation

With respect to the wave generation simulation, the numerical wave tank is divided into two regions: the wave-making region and the damping region; their lengths are 700 and 300 m, respectively, as shown in Figure 4. To fully consider the height of the water surface of the floating turbine, the air layer thickness above the water surface is set to 360 m, and the water depth below is set to 130 m. In terms of the simulation, a constant density Eulerian multiphase flow model is applied in the vertical direction of the tank. The region above the water surface is defined as air, whereas the region below the water surface is defined as water.

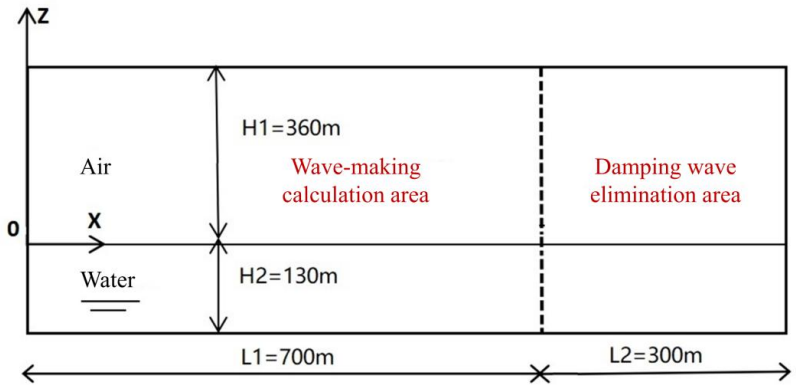

Fig. 4 Numerical tank spatial zoning

Mooring design

The selection of the mooring material is governed by the environmental loading characteristics and the mechanical properties of the composite floating structure. The selected mooring material is R4 grade studless offshore chain constructed of high-strength quenched and tempered steel, with a yield strength of ≥690 MPa, outstanding fatigue resistance, and remarkable seawater corrosion resistance. The Semi-Taut Mooring System is used to mitigate the dynamic impact load at the connection point of the UHPC float and complement the low ductility characteristics of its quasibrittle material. A pretension of 8.2×10^5 N was applied to each mooring line at the fairleads to provide the platform with initial restoring stiffness. The configuration of the mooring system is critical in ensuring the global stability of the floating platform. Therefore, six mooring chains are symmetrically arranged along the Y axis on both sides of the floating turbine. This arrangement provides consistent mooring support and decreases the offset and tilt of the turbine, effectively reducing the amplification of the mooring chain dynamics caused by the low-frequency movements of the UHPC floats (as shown in Figure 5). The specific parameters of the anchor chain material are listed in Table 3, the key parameters of the mooring system are provided in Table 4, and the coordinates of the mooring and anchor points are listed in Table 5. The system is simulated in the CFD solver, and the mooring system of the wind turbine is shown in Figure 6.

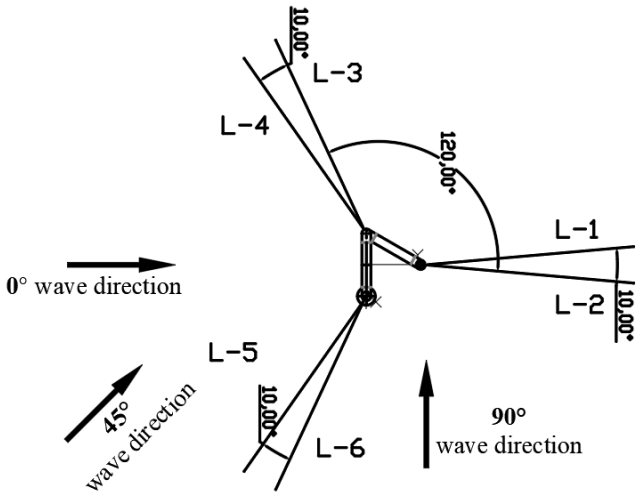

Fig. 5 Mooring system arrangement

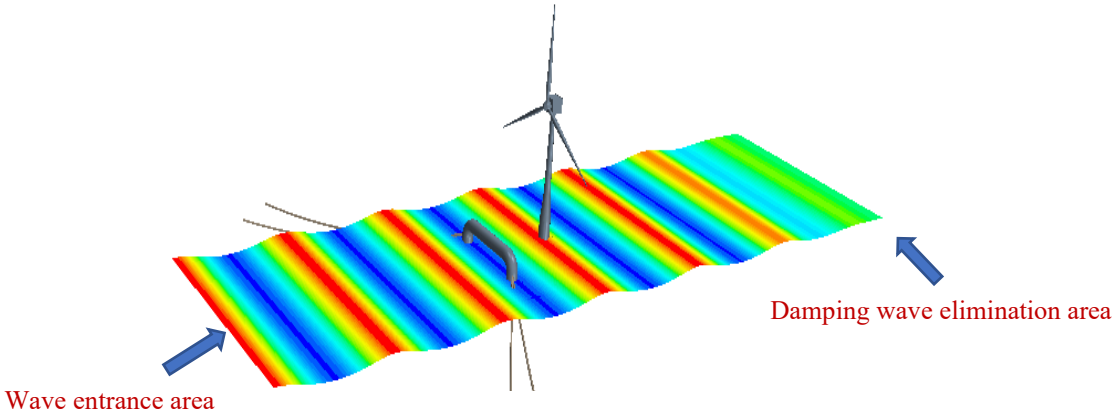

Fig. 6 Mooring system of the wind turbine in the CFD solver

Table 3 Mooring material parameters

Type	Diameter (mm)	Line weight (kg/m)	Axial stiffness (N)	Breaking strength (N)
R4 marine gearless anchor chain	95	158.5	9.025×10^8	9.002×10^6

Table 4 Mooring system parameters

Mooring method	Cable angle (°)	Quantity	Anchor radius (m)	Length (m)
Tension type	10	6	350	356

Table 5 0-degree mooring point and anchor point coordinates

Anchor chain number	Mooring point coordinates			Anchoring point coordinates		
	X (m)	*Y* (m)	*Z* (m)	*X* (m)	*Y* (m)	*Z* (m)
L-1	-98.43	0	30	-447.1	-30.5	-30
L-2	-98.43	0	30	-447.1	30.5	-30
L-3	3.75	-59	30	151.67	-376.2	-30
L-4	3.75	-59	30	204.49	-345.7	-30
L-5	3.75	59	30	204.49	345.7	-30
L-6	3.75	59	30	151.67	376.2	-30

3.3 Verification of grid convergence

The accuracy of the grid is crucial for wave generation in a numerical tank. Therefore, a grid convergence study is conducted prior to the simulations to determine the most appropriate grid size. The basic sizes of the computational domain are 8, 10, and 12 m, respectively. The total number of cells corresponding to the three different sizes (including only the grids of the computational domain and the water level-encrypted portion) are 2,799,000, 1,451,000, and 849,000, respectively. The wave simulation results and the positions of the two wave gauges are shown in Figure 7.

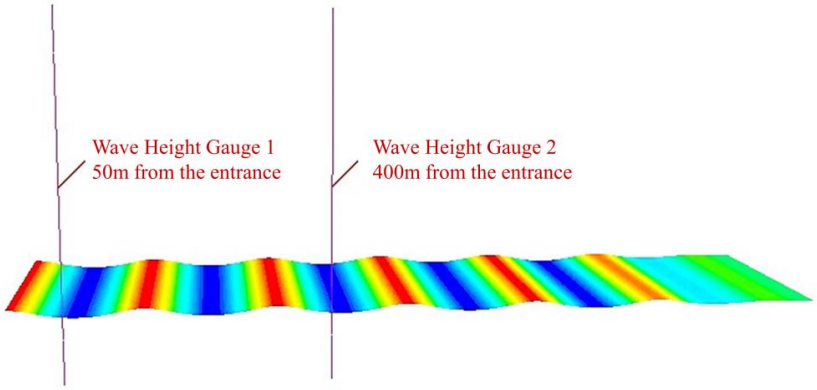

Fig. 7 Position of the wave altimeter

The two wave height gauges are positioned 50 and 400 m from the velocity inlet, and wave height gauge 2 is located at the origin position of the floating turbine (as shown in Figure 8). The time–history curves of wave height recorded by the wave height gauges at different locations are shown in the figure. Additionally, the numerical waves simulated with grid sizes of 8 and 10 m exhibit a high degree of similarity to the theoretical values. Considering the computational time and accuracy requirements, a grid size of 10 m is chosen as the basic size for the computational domain grid. Consequently, the basic size of the subtractive operation grid is 2.5 m.

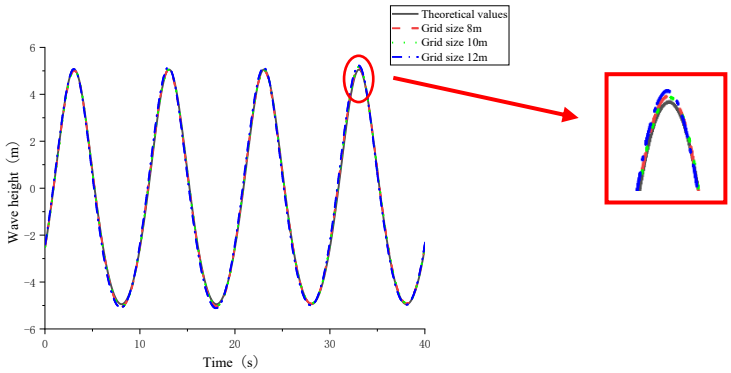

(a) Wave height of Gauge 1

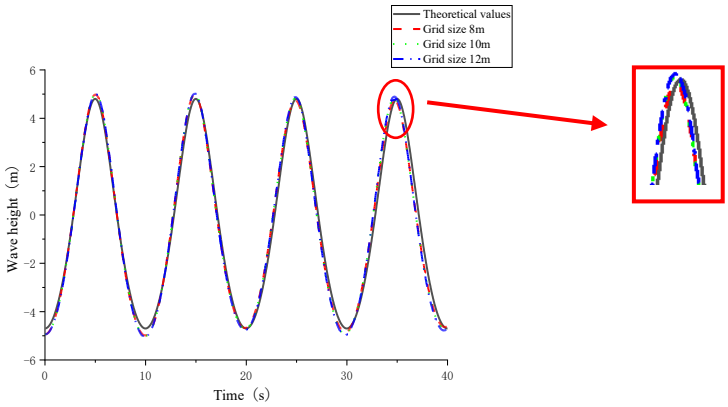

(b) Wave height of Gauge 2

Fig. 8 Wave height–time domain curve

4. Tank experiment

4.1 Experimental design

In this study, a physical-scale model experiment of a floating wind turbine was conducted in a wind–wave–current tank at Jiangsu University of Science and Technology. The tank is 38 m long, 15 m wide, and 1 m deep. Considering the specific limitations of the tank depth, a floating wind turbine model with a scale ratio of 1:68.5 was designed in accordance with similarity laws. To decrease wave reflections and ensure experimental reliability, a mesh-type wave dissipation system was installed on both sides of the tank, and an inclined mesh-type wave dissipation device was installed at the aft end. The measurement system consisted of an optical six-degree-of-freedom motion monitoring system, shore-based video-recording equipment, a wave height recorder, and a pressure transducer (as shown in Figure 9 in terms of the overall setup of the model experiment).

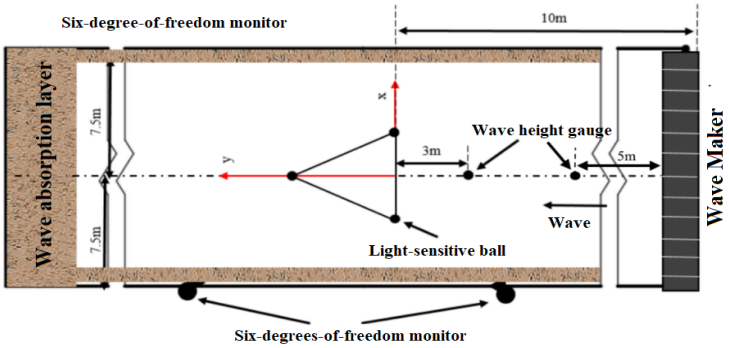

Fig. 9 General layout of the model experiment

In practical applications, the operating condition of a wind turbine is significantly affected by wind load. To accurately represent wind loading in the experiment, a ducted fan is used in this study to mimic the wind load and simulate its effect on the wind turbine. The ducted fan is capable of generating variable levels according to the experimental requirements. The installation location of the ducted fan is shown in Figure 10. The underlying principle is to simplify the external wind loads acting on the turbine as an equivalent reverse thrust applied to the floating platform by the ducted fan. The wind load on the full-scale turbine at a given wind speed is calculated using an empirical formula based on the projected area of the turbine components above the waterline. This wind load is then equivalent to the thrust generated by the ducted fan. When these two thrusts are equal, the effect of the ducted fan on the model turbine is considered equivalent to the wind load on the full-scale turbine. Notably, this approach does not satisfy Reynolds scaling for detailed aerodynamic simulation, which is acceptable for the present study, which focuses on structural response.

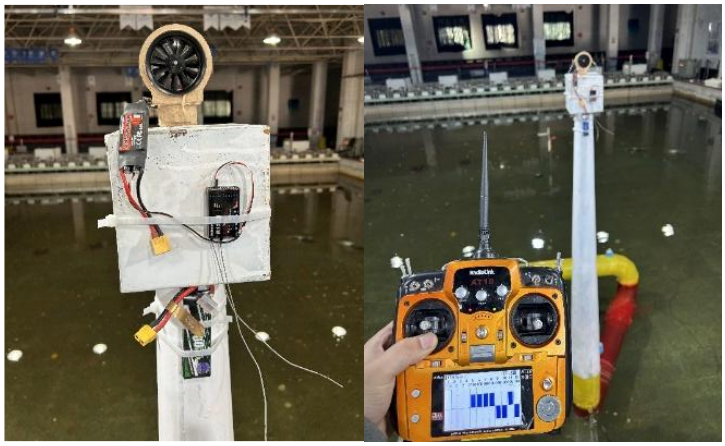

Fig. 10 Ducted fan and remote control equipment

To determine the characteristics of wave impact loads, measurement points were carefully placed in the key components of the floating platform within both the physical and numerical simulation models. This method was employed to investigate the wave impact characteristics and then validate the accuracy of the numerical model. With respect to the floating wind turbine platform experiment, eight pressure points were selected.

Table 6 lists the coordinates of the pressure monitoring points implemented in the floating turbine experimental model. The pressure sensors used were CY302 with a range of 0–100 kPa and an accuracy of 0.1 %. The locations of the monitoring points are shown in Figure 11. Table 7 lists the coordinates of the mooring points and anchor chains used in the experiment.

Table 6 Model monitoring point coordinates

Measuring point	*X* (m)	*Y* (m)	*Z* (m)
P1	0.109	0.336	0.672
P2	0	0.292	0.562
P3	-1.218	0	0.511
P4	-1.218	0	0.474
P5	-1.218	0	0.401
P6	0.109	-0.336	0.672
P7	0	-0.292	0.562
P8	0.077	0.844	0.438

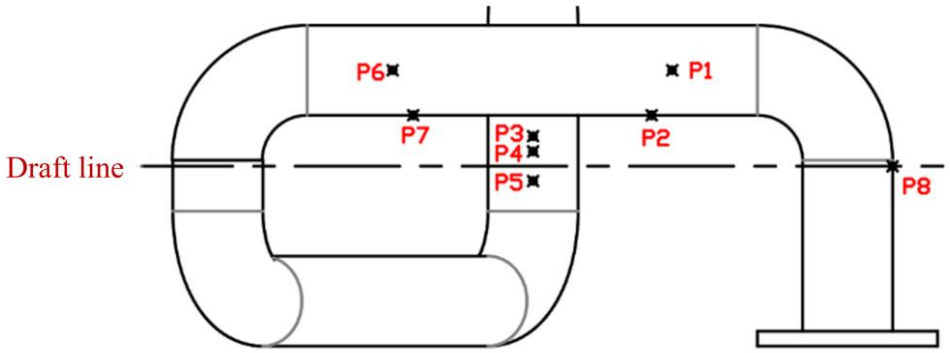

Fig. 11 Monitoring point locations

Table 7 Mooring point and anchor point coordinates

Anchor chain number	Mooring point coordinates			Anchor point coordinates		
	X (m)	*Y* (m)	*Z* (m)	*X* (m)	*Y* (m)	*Z* (m)
L1	-1.437	0	0.438	-6.527	-0.445	-0.438
L2	-1.437	0	0.438	-6.527	0.445	-0.438
L3	0.055	-0.861	0.438	2.214	-5.492	-0.438
L4	0.055	-0.861	0.438	2.985	-5.047	-0.438
L5	0.055	0.861	0.438	2.985	5.047	-0.438
L6	0.055	0.861	0.438	2.214	5.492	-0.438

4.2 Verification of natural period

The natural period of a floating body is a key indicator of its motion characteristics. To further verify the accuracy of the numerical model, the natural periods of sway, surge, and yaw motions of the wind turbine were analysed, as shown in Figure 12. The attenuation amplitudes and periods obtained from the experiments are consistent with the numerical simulation results, with period deviations within 10 % and amplitude deviations within 15 %. Moreover, the damping ratio *D* is calculated using Equation (10):

$$D = \frac{\lg \varphi}{\sqrt{0.1862 + (\lg \varphi)^2}} \tag{10}$$

where φ represents the ratio of the peak values of two neighbouring waveforms, $\varphi = \frac{|A_K| + |A_{K+1}|}{|A_{K+1}| + |A_{K+2}|}$. See Table 8 for details.

Table 8 Comparison of attenuation deviations

Motion response	Model experiment (s)	Numerical simulation (s)	Attenuation period deviation (%)	Amplitude deviation (%)	Damping
Swaying	221.45	240.31	7.85	12.17	0.1009
Surging	200.15	205.75	2.72	6.80	0.1749
Yawing	345.27	333.96	3.39	10.53	0.2194

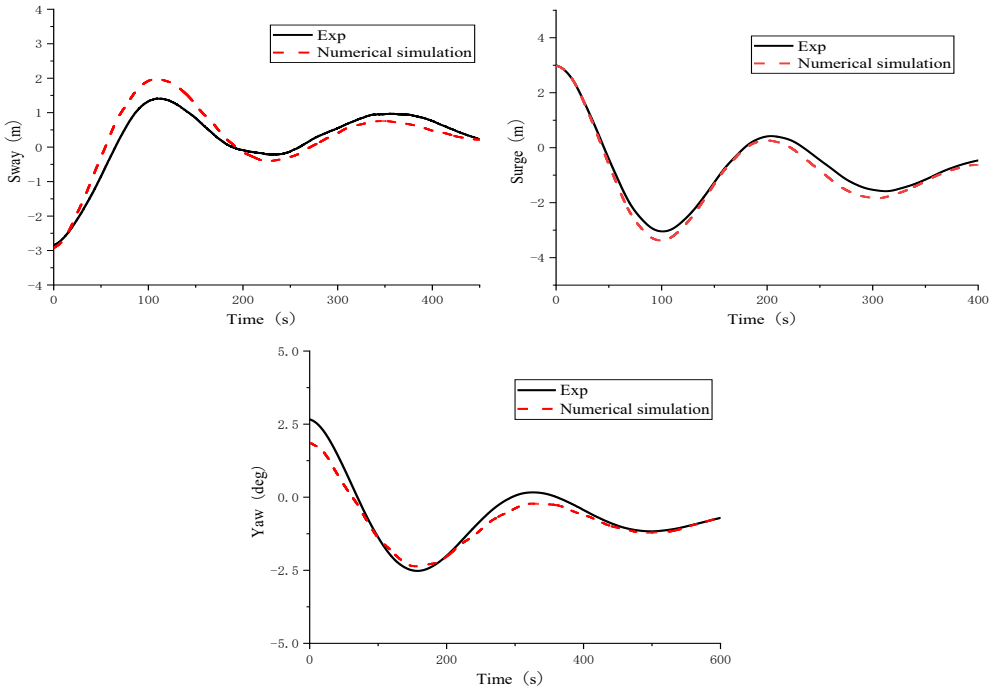

Fig. 12 Comparison of attenuation deviations

4.3 Comparison of the pressure data

The accuracy of the numerical simulation is assessed by comparing the experimental data with the pressure–time curves obtained from the numerical simulation under identical conditions. In this study, the data collected from the two measurement points, P4 and P5, were compared.

To analyse the experimental results for the slamming pressure of measurement point P4, these results are compared with the numerical simulation results under operating conditions with a wave height H= 8 m, a wave period T= 9 s, and a wind speed of 30 m/s. The results of this analysis are presented in Figure 13.

(1) Both numerical and experimental results exhibit consistent pressure trends at measurement point P4.

(2) The three steady maximum pressures measured experimentally are 75.77, 77.27, and 78.84 kPa. The corresponding numerical simulation results are 83.59, 78.97, and 74.33 kPa. The corresponding deviations are 9.36, 2.15, and 6.07 %, all of which fall within the range of acceptable deviations.

(3) The average period of the maximum pressure value in the experiment is 9.1 s, whereas the numerical simulation results are 9.15 s. The deviations from the theoretical period of 9 s are 1.11 and 1.67 %, which are sufficiently small and acceptable.

To analyse the experimental results for the slamming pressure of measurement point P5, these results are compared with the numerical simulation results under operating conditions with a wave height H= 8 m, a wave period T= 10 s, and a wind speed of 30 m/s. The results of this analysis are presented in Figure 13.

(1) Both the numerical and experimental results exhibit consistent pressure trends at measurement point P5.

(2) The three steady maximum pressures measured experimentally are 91.76, 90.03, and 89.14 kPa. The corresponding numerical simulation results are 87.81, 87.65, and 84.78 kPa. The corresponding deviations are 4.51, 2.72, and 5.14 %, all of which fall within the range of acceptable deviations.

(3) The average period of the maximum pressure value in the experiment is 9.98 s, whereas the numerical simulation results are 9.94 s. The deviations from the theoretical period of 10 s are 0.2 and 0.6 %, which are sufficiently small and acceptable.

On the basis of the comparative analysis of pressure trends, peak values, and their characteristic periods, the numerical simulation framework provides accurate and reliable predictions.

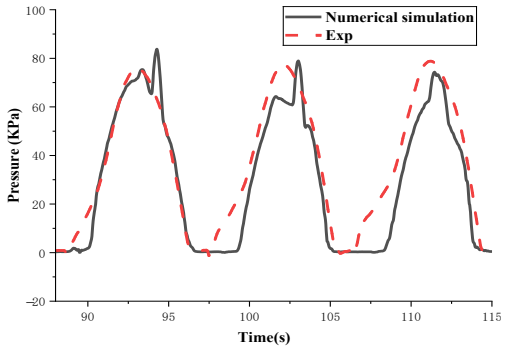

(a) Slamming pressure of P4

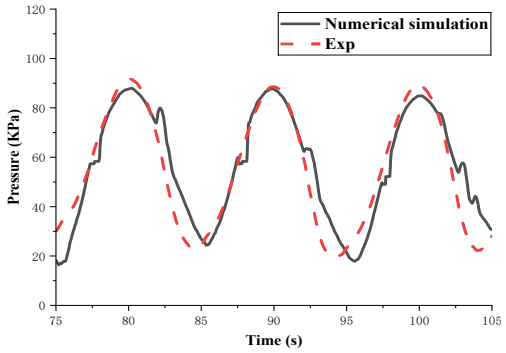

(b) Slamming pressure of P5

Fig. 13 Comparison of slamming pressure for P4 and P5

4.4 Structural design of steel–UHPC foundation

In this section, the structural design of the Moray Base floating wind turbine is developed on the basis of the environmental conditions of the installation site and the structural characteristics of the turbine, with steel–UHPC used as the primary construction material, as shown in Figure 14. The material and size of the main components are shown in Table 9. The transverse bulkhead, heave plate and floating foundation are reinforced concrete structures. The concrete is UHPC, and the reinforcement is hot-rolled ribbed bar HRB series. In accordance with the design requirements, the steel bar grades of HRB400 and HRB500 are selected for the plate-type components at different positions. The remaining components of the floating wind turbine are designed as steel structures. To improve local structural stability, multiple internal bulkheads are arranged within the cabins. The length of the two main cabins is 75 m, which is easily affected by the mid-arch and sagging. Because the torsion force of the four elbows under wave action is large, the subdivision is designed to further strengthen the structure. In addition, at the mooring position, the bulkhead is also used for reinforcement to mitigate the larger mooring force.

Considering constructability and structural performance, the design strictly adheres to the relevant provisions of the specification 'DNV-OS-C502 2012-09 Offshore Concrete Structures' of the Norwegian Classification Society. Considering the simplicity of practical engineering analysis and numerical simulation, the thickness of reinforced concrete protective layer was standardized to 50 mm, and the spacing of steel bars was uniformly set to 100 mm. The specific reinforced structure is shown in Figure 15.

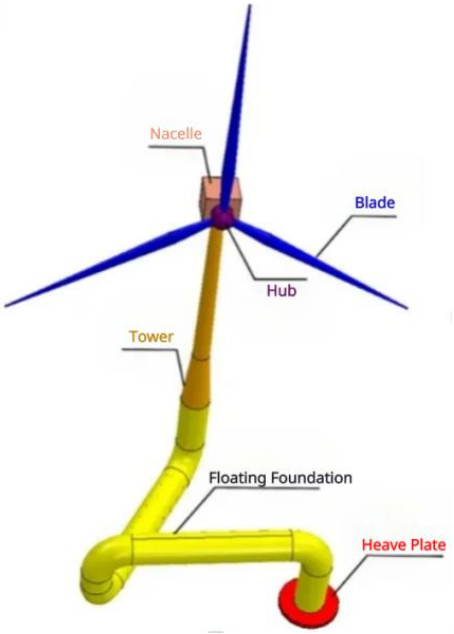

Fig. 14 Floating wind turbine structure

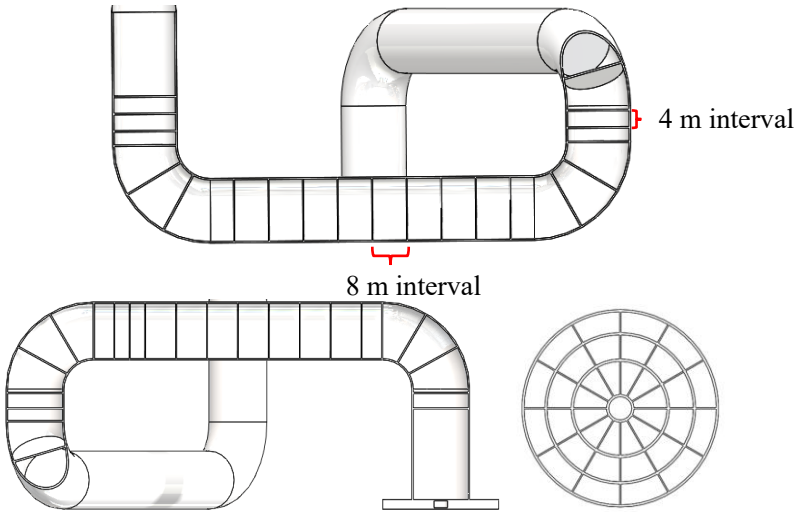

Fig. 15 Bulkhead reinforcement structure

Table 9 Structural dimensions of the wind turbine

Structure	Material	Thickness or diameter (mm)
Heave plate outer plate	UHPC	380
Transverse bulkhead reinforcement of the heave plate	UHPC	200
Ring bulkhead reinforcement of the heave plate	UHPC	380
Floating foundation outer plate	UHPC	380
Mooring position, Bulkhead at the bend pipe	UHPC	380
Other bulkheads	UHPC	200
Tower	AH36	20
Nacelle	AH36	28
Hub	AH36	24
Blade	AH36	10
380 mm double-layer reinforced concrete bars	HRB500	40
200 mm concrete single-layer rebar	HRB400	30

4.5 Equivalent simulation of steel–UHPC constitutive relation

On the basis of the constitutive modelling approach for concrete proposed by Vorel et al. [27], the equivalent elastic modulus (E) and equivalent yield strength (fs) of steel–UHPC members are determined

using an equivalent material model. Within the finite-element software environment, an analytical model is established to evaluate the performance of steel–UHPC structures. The plate thickness and reinforcement are determined according to the design values, and the specific parameters of different plate thicknesses are listed in Table 10. The stress–strain responses of reinforced-concrete members are obtained by applying prescribed displacement loads. The resulting equivalent stress–strain behaviour relies on both the plate thickness and the reinforcement characteristics. Consequently, equivalent continuum elements are derived on the basis of the different characteristics of the members in the table. Considering that the floating platform has a diameter of 15 m and a large outer plate curvature, a flat plate sample with dimensions of 2×1 m is selected to represent the member in the material equivalence procedure. Figure 16 presents the isolated finite element model and the equivalent principal constitutive curve of the member with a plate thickness of 380 mm. The curve indicates that the inflection point of the stress–strain relationship corresponds to the yield strain of the reinforcement, and the yield strain of HRB500 is 0.0024. The elastic modulus of the equivalent material is the ratio of the equivalent yield strength to the reinforcement yield strain. The calculation method for the yield strength of HRB400 is identical to that of HRB500. On the basis of the stress–strain curve calculated above, the physical and mechanical parameters of different members after equivalence can be derived as presented in Table 11. Detailed descriptions of the equivalent material modelling parameters and the treatment of experimental uncertainties are provided in the Supplementary Material.

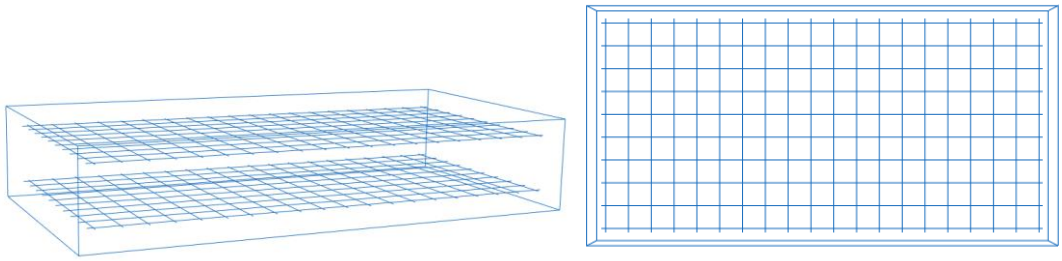

(a) Separate finite element model

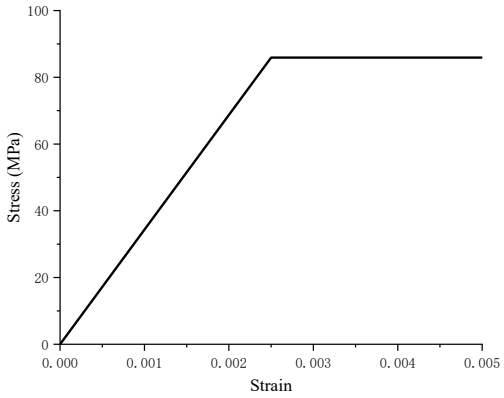

(b) Equivalent constitutive curve

Fig. 16 Separated finite element model and equivalent constitutive curve of 380 mm thick plate members

Table 10 Plate thickness and reinforcement parameters

Shape	Thickness (mm)	Reinforcement	Reinforcement	Reinforcement	Steel	Reinforcement
Plate	200	Single layer	36	100	HRB400	5.09
Plate	380	Double layer	40	100	HRB500	8.11

Table 11 Equivalent elastic modulus and yield strength of steel–UHPC with different plate thicknesses

Component thickness (mm)	Equivalent elastic modulus (MPa)	Equivalent yield strength (MPa)
200	1.4×10^4	26.33
380	3.6×10^4	85.91

4.6 Verification of grid division and convergence

4.6.1 Grid division

Selecting an appropriate mesh size and density to achieve a balance between computational accuracy and efficiency is a critical task in finite element analysis. The meshed finite element model of the floating wind turbine is shown in Figure 17.

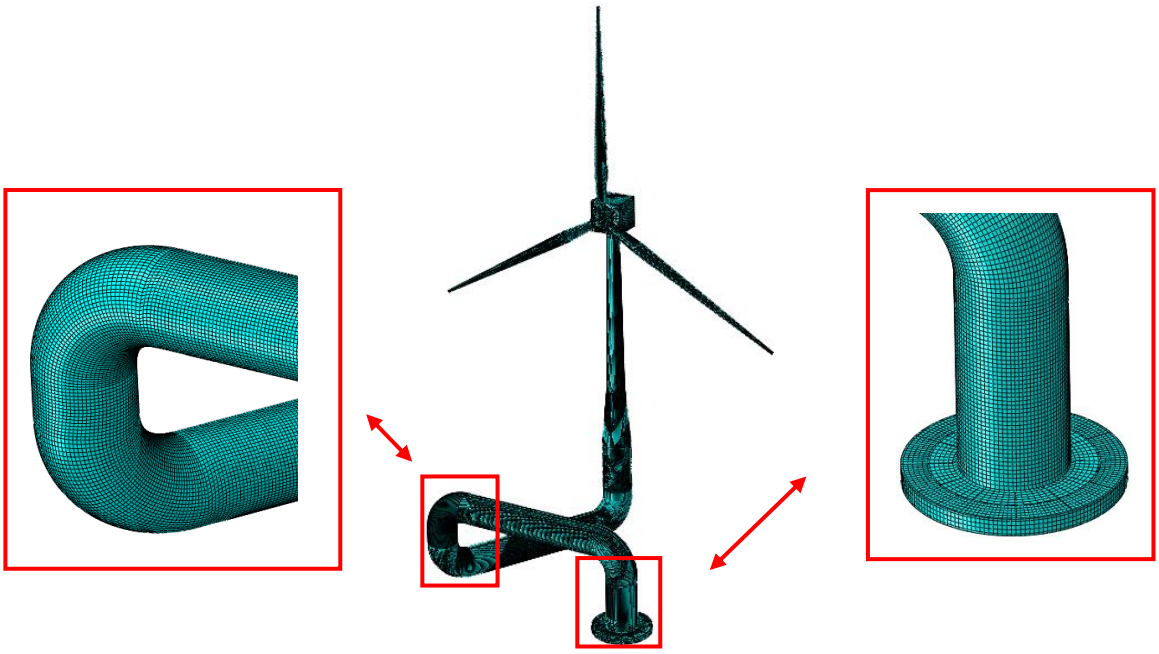

Fig. 17 Finite element mesh division and its detailed diagram

4.6.2 Verification of grid convergence

In this section, a mesh sensitivity analysis is performed to determine the optimal mesh size. This task is achieved by verifying the mesh sensitivity of the finite element model under the condition of only gravity acting. The calculation results corresponding to different numbers of meshes are presented in Table 12. As shown in Figure 18, the range from 0.4 to 0.8 m is recognized as the stable section. Considering both computational efficiency and accuracy, a global mesh size of 0.6 m is selected for subsequent analyses.

Table 12 Calculation results and number of grids

Approximate global size (m)	Maximum stress (MPa)	Number of C3D8R element types	Number of C3D6 element types	Total elements
0.4	74.37	275414	34910	310324
0.6	74.27	122096	23031	145127
0.8	75.91	55406	19937	75343
1	84.19	47993	8268	56261
1.2	91.79	46202	3759	49961

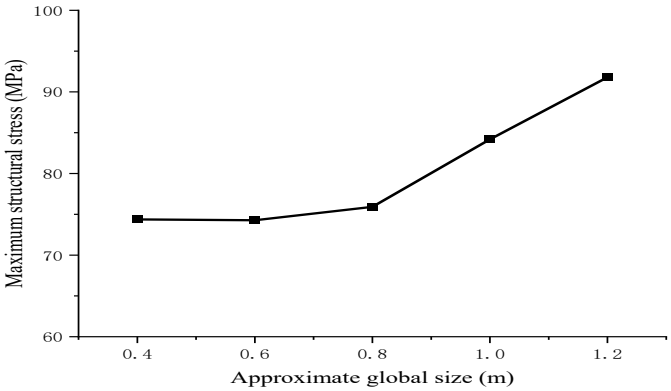

Fig. 18 Variation in maximum stress with the approximate global size

4.7 Strength check

4.7.1 Safety factor and evaluation of the working condition

On the basis of the DNV specification, a 50-year return period sea state is used as the basis for the study. The selected conditions represent a parked turbine survival scenario with H=11 m, T=12 s, wind speed of 35 m/s, current speed of 1.5 m/s, wave direction angles of 0, 45, and 90°, and working water depth of 60 m. The specific parameters of each load case are presented in Table 13.

In accordance with 'DNV-OS-C502 2012-09 Offshore Concrete Structures', establishing a safety factor for the material parameters is essential, considering the uncertainties associated with material strength and section dimensions. To evaluate the material strength under extreme sea conditions, a range of material coefficients needs to be considered. In this study, the main body of the wind turbine is constructed of reinforced-concrete material, and the steel bars mainly bear tension. Accordingly, when the strength of the wind turbine under extreme sea states is checked, the safety factor method is employed, and the safety factor is 1.25. The converted results are presented in Table 14.

The simulation time for each load case was 60 s. This duration encompasses five complete wave cycles (T=12 s). With respect to the ultimate strength assessment, this simulation duration is sufficient to capture the quasisteady extreme responses of interest. This duration is validated by the data in Table 15, which shows that the maximum stress occurs between 49.27 and 54.75 s across different cases. This finding indicates that the peak stresses were captured during the well-developed phase of the dynamic response, not during the initial transient phase, thus confirming the adequacy of the simulation time for this ultimate limit state assessment. Although the final design certification requires a comprehensive irregular wave analysis, the use of a representative “design wave” is a well-established engineering practice for preliminary ultimate strength and global strength assessment, because it efficiently identifies critical load patterns and governing structural responses. Future work will employ longer time-domain simulations for long-term fatigue analysis under irregular waves.

Table 13 Strength check conditions

Working condition	*H* (m)	*T* (s)	Velocity (m/s)	Wind speed (m/s)	Wave direction angle (°)
A1	11	12	1.5	35	0
A2	11	12	1.5	35	45
A3	11	12	1.5	35	90

Table 14 Yield strength after the conversion of the safety factor

Thickness of the plating (mm)	Equivalent yield strength (MPa)	Converted safety factor (MPa)
200	26.33	21.06
380	85.91	68.73

4.7.2 Overall structural strength check of floating platform

The hydrodynamic load setting and structural design of the floating wind turbine are described above. The structural strength of the floating wind turbine platform is subsequently evaluated under severe sea states with different wave directions. With respect to the CFD solver, the hydrodynamic model incorporating the mooring system is subjected to external environmental loads, including wind, waves, and currents. This process enables the calculation of the surface-acting load of the floating wind turbine. The obtained loads are then transferred to the FEA solver as boundary conditions using the CFD–FEA one-way coupling calculation method. With respect to the FEA solver, the mooring tension is applied as a concentrated nodal force at the corresponding cable attachment points, and its direction is updated according to the instantaneous platform motion. Moreover, the structural body, gravitational load, and boundary constraints of the floating wind turbine are constructed in the FEA solver, and the displacement boundary condition is spring-loaded moorings. According to the CFD–FEA coupling calculations, the maximum structural stresses and maximum equivalent stresses for each working condition are presented in Table 15.

After the upper limit of the equivalent stress is set to 68.73 MPa, the equivalent stress cloud map of the 45° wave downwards is shown in Figure 19. An inspection of the equivalent stress cloud of the wind turbine platform indicates that, except for the mooring location, all other points satisfy the specified strength requirements. The elevated stresses at the mooring locations are primarily associated with localized load transfer effects and are beyond the scope of the present study.

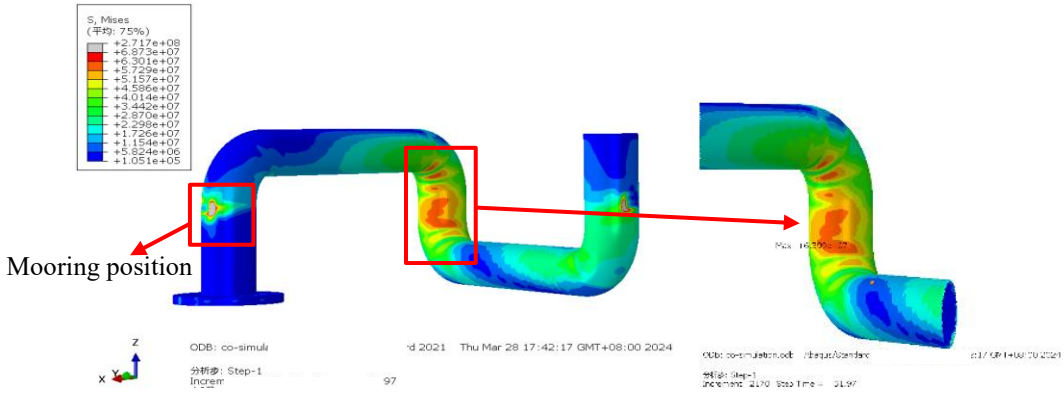

(a) Stress cloud diagram of the floating platform outer plate

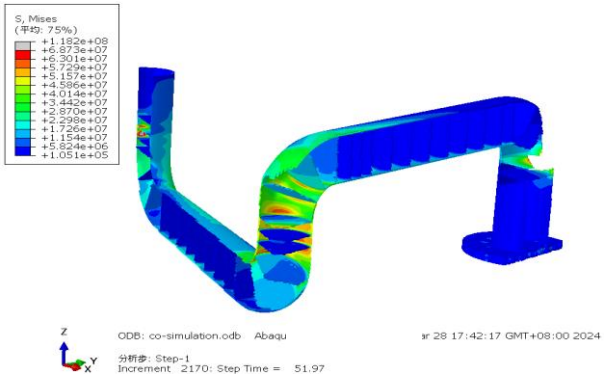

(b) Stress cloud diagram of the floating platform reinforced bulkhead

Fig. 19 Stress cloud diagram of equivalent structure of floating platform in 45° wave direction maximum stress time

As shown in Table 15, under a wave direction of 45°, the maximum equivalent stress of the component with a plate thickness of 380 mm reaches 63.99 MPa. Combined with the equivalent elastic modulus of 3.6×10^4 MPa listed in Table 11, the corresponding maximum strain can be calculated as $\varepsilon_{max}=\sigma_{max}/E\approx0.178\%$. This value is lower than 0.2 %, thereby fully satisfying the applicability criterion for one-way coupling specified in the reference cited in Section 2.3 [26], which confirms the validity of the numerical approach adopted in this study.

Table 15 Strength check results of floating platform under various working conditions

Working condition	Different plate thickness (mm)	Maximum stress time (s)	Maximum equivalent stress (MPa)	Equivalent strength (MPa)	Checking results
A1	200	54.75	15.36	21.06	Safety
	380		43.27	68.73	Safety
A2	200	51.97	20.35	21.06	Safety
	380		63.99	68.73	Safety
A3	200	49.27	18.57	21.06	Safety
	380		61.63	68.73	Safety

4.8 Comparison of steel–UHPC with traditional materials

The results of the above analysis indicate that the strength of the floating foundation meets the required standards. This study provides a foundation for replacing steel structures with steel–UHPC as the preferred manufacturing material for marine floating structures. The advantages of the reinforced concrete floating wind turbine compared with a traditional all-steel design are summarized in Table 16.

Table 16 Comparison between steel structures and concrete

Comparison category	Steel construction	Steel–UHPC
Usage	Susceptible to corrosion, requires daily maintenance	Corrosion and oxidation resistance is stronger, and maintenance costs are generally lower.
Environmental protection	Requires regular coating or anticorrosion treatments, which may pose environmental concerns	No regular painting or anticorrosion treatment is required.
Structure	Under severe weather conditions, the wind turbine foundation is prone to vibration deformation.	Higher global stiffness and stability effectively mitigate platform vibration and deformation during operation.
Cost	The material cost of the conventional steel structure floating foundation material of the Moray Base is approximately 49.2 million.	The material cost of reinforced concrete floating foundation material designed in this study is approximately 35.6 million.

In terms of construction cost, compared with the conventional steel structure, the floating platform in this study achieves a 27.6 % reduction in material cost. This does not include other costs saved during the construction process. The stated 27.6 % reduction in material cost is derived from a comparison between two designs that both comply with the same safety standards and are designed to withstand the same 50-year return period environmental conditions. The conventional steel design serves as the baseline and satisfies strength requirements when AH36 steel with industry-standard safety factors is used. The proposed steel–UHPC design is an alternative solution that meets the same functional and safety requirements, as confirmed in Section 5.4 using a material safety factor of 1.25 as per DNV-OS-C502. The cost calculation is based on the material quantities listed in Table 9 and current market prices for steel and UHPC/concrete, providing a fair comparison of material cost efficiency between the two structurally equivalent solutions.

Compared with traditional steel designs, reinforced concrete floating wind turbines have distinct advantages in terms of durability, resistance to extreme environmental loads, environmental sustainability, and overall cost efficiency, particularly for long-term offshore applications.

5. Conclusion

This study presents a structural safety assessment of a steel–UHPC floating foundation for the Moray Base wind turbine under extremely regular wave conditions using a combined numerical and experimental approach. The one-way CFD–FEA coupling method was validated through tank experiments, which revealed its accuracy in predicting wave loads and structural responses for the designed composite structure. The structural design and strength under the extreme sea state 50-year return period were confirmed to meet the safety requirements specified by the DNV code.

The proposed steel–UHPC solution demonstrates a viable pathway to achieve this by significantly decreasing material costs and lifetime maintenance expenses because of its superior corrosion resistance. This transition from traditional all-steel designs to high-performance concrete composites could be pivotal for improving the economic feasibility of next-generation large-scale floating wind farms, particularly in harsh marine environments.

Despite these advantages, practical deployment must still address challenges such as the high precision required for offshore construction of large UHPC elements and the logistical planning associated with their substantial structural mass. Nonetheless, the transition to this material system represents a viable path towards more economical and durable floating wind solutions.

While this study focused on ultimate strength under extreme loads, the commercialization of steel–UHPC floating foundations requires further investigation. On the basis of the outcomes of this work, the following directions for future research are proposed:

1 Long-term fatigue analysis of floating foundations under irregular wave spectra.

2. Two-way coupled CFD–FEA for extreme and failure scenarios.

This work not only validates the structural safety of a novel steel–UHPC floating foundation but also highlights its potential to reduce costs and improve durability in offshore wind applications. By addressing the identified research challenges, the offshore wind industry can move closer to the widespread use of this promising technology.

APPENDIX

Equivalent Material Modeling parameter and Experimental Uncertainty

A1. Equivalent Material Modeling for Steel-UHPC Components

A1.1 Constituent Material Properties

The equivalent model is derived from the separate behaviors of UHPC and the steel reinforcement bars. The key material parameters used in the ABAQUS finite element model are as follows:

UHPC Material Model:

Density: 2400 kg/m³

Elastic Modulus (E_c):60 GPa

Poisson's Ratio (υ_c): 0.2

Tensile Strength: 21.9 MPa (This value was adopted as the yield strength of UHPC in the equivalent model, based on the bending test results provided by Shafieifar et al. [28]).

Steel Rebar Material Model:

Density: 7850 kg/m³

Elastic Modulus (E_s): 210 GPa

Poisson's Ratio (υ_s): 0.3

Tensile Strength:

(1) HRB400: 400 MPa

(2) HRB500: 500 MPa

A2. Characterization of Experimental Uncertainty

A2.1 Wave Gauge

Type: Capacitive Wave Height Meter

Measurement Range: -250 to +250 mm

Accuracy: < ±0.5% of the reading

A2.2 Optical Motion Capture System (for 6-DOF Decay Tests)

Measured Degrees of Freedom:

Surge, Sway: ±180° within 10 m

Heave: ±1 m

Roll, Pitch: ±90°

Yaw: ±180°

Accuracy:

Displacement (Surge, Sway, Heave): ±2 mm.

Rotation (Roll, Pitch, Yaw): ±0.1°

A2.3 Tension Transducers (for Mooring Line Tension)

Measurement Range: 1 to 20 kg (scaled model)

Accuracy: ±0.25 % of Full Scale

Sensitivity: 1.133 mV/V

REFERENCES

[1] Oh, S., 2021. Comparison of concrete and steel semi-submersible floaters for 10MW wind turbines. *Journal of Physics: Conference Series*, 2021(1), 012029. https://doi.org/10.1088/1742-6596/2018/1/012029

[2] Zhu, J. X., Weng, K. F., Huang, B. T., Xu, L. Y., Dai, J. G., 2024. Ultra-High-Strength Engineered Cementitious Composites (UHS-ECC) panel reinforced with FRP bar/grid: Development and flexural performance. *Engineering Structures*, 302, 117193. https://doi.org/10.1016/j.engstruct.2023.117193

[3] Liao, J., Yang, K. Y., Zeng, J. J., Quach, W. M., Ye, Y. Y., Zhang, L., 2021. Compressive behavior of FRP-confined ultra-high performance concrete (UHPC) in circular columns. *Engineering Structures*, 249, 113246. https://doi.org/10.1016/j.engstruct.2021.113246

[4] Yao, Y., Mobasher, B., Wang, J., Xu, Q., 2021. Analytical approach for the design of flexural elements made of reinforced ultra-high performance concrete. *Structural Concrete*, 22(1), 298-317. https://doi.org/10.1002/suco.201900404

[5] Nie, J., 2020. Application of steel-concrete composite structure in ocean engineering. *Steel Construction*, 35(1), 20-33. http://gjg.ic-mag.com/en/article/doi/10.13206/j.gjgSE19112601

[6] Zheng, S, Zhang, Y, 2023. Hydrodynamic Characteristics of a Basalt Fiber Large-scale Marine Net Cage Under Typhoon Conditions of Level 17. *Ocean Development and Management*, 40(10), 129-136.

[7] Zeng, J. J., Hao, Z. H., Sun, H. Q., Zeng, W. B., Fan, T. H., Zhuge, Y., 2025. Durability assessment of ultra-high-performance concrete (UHPC) and FRP grid-reinforced UHPC plates under marine environments. *Engineering Structures*, 323, 119313. https://doi.org/10.1016/j.engstruct.2024.119313

[8] Walia, D., Schiinemann, P., Kuhl, M., Adam, F., Hartmann, H., Großmann, J., Ritschel, U., 2017. Prestressed ultra high performance concrete members for a TLP substructure for floating wind turbines. *The 27th International Ocean and Polar Engineering Conference (ISOPE)*, June 25-30, San Francisco, California, USA, ISOPE-I-17-304.

[9] Yan, Z., Zeng, J. J., Zhuge, Y., Liao, J., Zhou, J. K., Ma, G., 2024. Compressive behavior of FRP-confined 3D printed ultra-high performance concrete cylinders. *Journal of Building Engineering*, 83, 108304. https://doi.org/10.1016/j.jobe.2023.108304

[10] Hussain, A., Yu, T., Zou, F., 2025. Durability analysis of nanocarbon black-based self-strain sensing ultra-high-performance concrete (UHPC): Effects of moisture content and sea-salt solution exposure. *Construction and Building Materials*, 473, 141031. https://doi.org/10.1016/j.conbuildmat.2025.141031

[11] Jiao, J., Chen, Z., Xu, S., 2024. CFD-FEM simulation of water entry of aluminium flat stiffened plate structure considering the effects of hydroelasticity. *Brodogradnja*, 75(1), 75108. http://dx.doi.org/10.21278/brod75108

[12] Chen, Z., Jiao, J., Jiang, C., Si, H., Chen, S., 2024. Scale effects on wave loads and slamming loads in ship hydroelasticity simulation by CFD-FEM method. *Ocean Engineering*, 314, 119718. https://doi.org/10.1016/j.oceaneng.2024.119718

[13] Jiao, J., Huang, S., Tezdogan, T., Terziev, M., Soares, C. G., 2021. Slamming and green water loads on a ship sailing in regular waves predicted by a coupled CFD–FEA approach. *Ocean Engineering*, 241, 110107. https://doi.org/10.1016/j.oceaneng.2021.110107

[14] Jia, G., Jiao, J., Chen, C., Wu, T., 2025. CFD simulation of wave-induced motions of an LNG ship considering tank sloshing effects. *Brodogradnja*, 76(3), 76307. http://dx.doi.org/10.21278/brod76307

[15] Kale, F. M., Yilmaz, N., Sokmen, K. F., Shi, W., 2025. Experimental and numerical investigations of hydrodynamic performance for horizontal-axis hydrokinetic turbines. *Brodogradnja*, 76(3), 76308. http://dx.doi.org/10.21278/brod76308

[16] Lakshmynarayanana, P. A., Temarel, P., 2020. Application of a two-way partitioned method for predicting the wave-induced loads of a flexible containership. *Applied Ocean Research*, 96, 102052. https://doi.org/10.1016/j.apor.2020.102052

[17] Lakshmynarayanana, P. A. K., Hirdaris, S., 2020. Comparison of nonlinear one-and two-way FFSI methods for the prediction of the symmetric response of a containership in waves. *Ocean engineering*, 203, 107179. https://doi.org/10.1016/J.OCEANENG.2020.107179

[18] Li, H., Han, B., Liu, S., Chen, S., Wang, Z., Deng, B., 2024. A review of the numerical strategies for solving ship hydroelasticity based on CFD-FEM technology. *Ships and Offshore Structures*, 19(11), 1912-1930. https://doi.org/10.1080/17445302.2024.2317040

[19] Löhner, R., Cebral, J. R., Yang, C., Baum, J. D., Mestreau, E. L., Soto, O., 2006. Extending the range and applicability of the loose coupling approach for FSI simulations. *Fluid-Structure Interaction*, 53, 82-100. https://doi.org/10.1007/3-540-34596-5_4

[20] Ding, D., Ouahsine, A., Xiao, W., Du, P., 2021. CFD/DEM coupled approach for the stability of caisson-type breakwater subjected to violent wave impact. *Ocean Engineering*, 223, 108651. https://doi.org/10.1016/j.oceaneng.2021.108651

[21] Lin, H., Luan, H., Uzdin, A. M., Zhang, S., Wei, L., Yang, L., 2024. A CFD-FEA coupled model for simulating dynamic response of offshore jacket platform under earthquake considering wind, wave, current and aftershock loads. *Ocean Engineering*, 300, 117481. https://doi.org/10.1016/j.oceaneng.2024.117481

[22] Yu, H., Xiang, G., Li, Y., Zhou, H., Yu, X., 2024. Trajectory simulation of 3D-printed container models based on CFD. *Ocean Engineering*, 291, 116489. https://doi.org/10.1016/j.oceaneng.2023.116489

[23] Yin, Z., Li, G., Wu, F., Ni, Z., Li, F., 2024. Experimental and numerical study on hydrodynamic characteristics of a bottom-hinged pitching flap breakwater under regular waves. *Ocean Engineering*, 293, 116665. https://doi.org/10.1016/j.oceaneng.2024.116665

[24] Jiang, Z., Li, F., Tavakoli, S., Kujala, P., Suominen, M., Hirdaris, S., 2024. A viscous investigation on the hydrodynamic coefficients and wave loads under the interaction of side-by-side cylinders in regular waves. *Ocean Engineering*, 297, 117156. https://doi.org/10.1016/j.oceaneng.2024.117156

[25] Xia, T. Y., 2021. Study on Structural Collapse Response of Ship Structure in Waves based on Coupling Simulation of CFD and Nonlinear Finite Element Method. *Wuhan University Of Technology.* Wuhan, China.

[26] Wijesooriya, K., Mohotti, D., Amin, A., Chauhan, K., 2021. Comparison between an uncoupled one-way and two-way fluid structure interaction simulation on a super-tall slender structure. *Engineering Structures*, 229, 111636. https://doi.org/10.1016/j.engstruct.2020.111636

[27] Vorel, J., Marcon, M., Cusatis, G., Caner, F., Di Luzio, G., Wan-Wendner, R., 2021. A comparison of the state of the art models for constitutive modelling of concrete. *Computers & Structures*, 244, 106426. https://doi.org/10.1016/j.compstruc.2020.106426

[28] Shafieifar, M., Farzad, M., Azizinamini, A., 2017. Experimental and numerical study on mechanical properties of Ultra High Performance Concrete (UHPC). *Construction and Building Materials*, 156, 402-411. https://doi.org/10.1016/j.conbuildmat.2017.08.170